

Topological Mott Insulator with Bosonic Edge Modes in 1D Fermionic Superlattices

Haiping Hu,¹ Shu Chen,^{2,3} Tian-Sheng Zeng,¹ and Chuanwei Zhang^{1,*}

¹*Department of Physics, The University of Texas at Dallas, Richardson, Texas 75080, USA*

²*Beijing National Laboratory for Condensed Matter Physics,*

Institute of Physics, Chinese Academy of Sciences, Beijing 100190, China

³*School of Physical Sciences, University of Chinese Academy of Sciences, Beijing, 100049, China*

We investigate topological phase transitions driven by interaction and identify a novel topological Mott insulator state in one-dimensional fermionic optical superlattices through numerical density matrix renormalization group (DMRG) method. Remarkably, the low-energy edge excitations change from spin-1/2 *fermionic* single-particle modes to spin-1 *bosonic* collective modes across the phase transition. Due to spin-charge separation, the low-energy theory is governed by an effective spin superexchange model, whereas the charge degree of freedom is fully gapped out. Such topological Mott state can be characterized by a spin Chern number and gapless magnon modes protected by a finite spin gap. The proposed experimental setup is simple and may pave the way for the experimental observation of exotic topological Mott states.

Introduction.—The interplay between single-particle band topology and many-body interaction plays a crucial role in many important strongly-correlated phenomena in condensed matter physics. Unlike single-particle topological states [1, 2], interactions can induce remarkable physical phenomena such as fractionalization of emergent collective excitations and give rise to intriguing correlated states that exhibit non-trivial topological properties. Prominent examples are fractional quantum Hall effects [3, 4] where constituent particles are electrons but emergent quasiparticles only carry fractions of electron charge, and topological Mott insulator [5] with deconfined spinon excitations.

One-dimensional (1D) interacting systems, which are amenable to exact methods, provide fundamental insights for understanding strongly-correlated states. Due to the confined geometry, the low-energy excitations are collective and exhibit a peculiar fractionalization, spin-charge separation (SCS). A single-particle excitation is divided into two collective modes, which possess charge and spin degrees of freedom, respectively. In a topological Mott insulator, low-energy excitations lie in the spin sector, whereas charge excitations are frozen by strong interactions. The topological properties manifest themselves by the appearance of gapless modes at the boundary protected by the insulating bulk. In previous studies, these edge modes are composed of spinons [6, 7] carrying spin-1/2 and no charge. As spinful modes can also carry integer spin (like magnon, spin-1), two natural and important questions need to be addressed: i) Are there topological Mott insulator states hosting other types of spinful edge modes and how to characterize them? ii) Since SCS severely changes the low-energy excitations, what is the bulk-edge correspondence in a topological Mott insulator state?

In this paper, we address these two important questions by studying the Mott insulator states in a 1D fermionic optical superlattice. Ultracold atoms in optical lattices have provided unprecedented controllability

to simulate strongly interacting systems. In particular, 1D optical superlattices open a new and simple avenue towards realizing exotic topological states [8–14] because of their exact correspondence with quantum Hall physics [15, 16] in an extended space. Here we scrutinize Mott transitions in 1D optical superlattices and identify a novel topological Mott insulator using the quasi-exact numerical density matrix renormalization group (DMRG). Such Mott phase transition from a band topological insulator to a topological Mott insulator is accompanied by bulk excitation gap closing, SCS, and the change of topological spin Chern number. The corresponding low-energy excitations change from single-particle spin-1/2 fermionic modes to collective spin-1 bosonic modes, in consistent with the spin Chern number change across the transition (*i.e.*, bulk-edge correspondence). The low-energy physics is governed by an antiferromagnetic spin superexchange model due to SCS. Our proposed experimental setup involves fermions in a 1D triple-well superlattice and is simple to realize in experiments comparing to other complex lattice models or materials [5–7].

Single-particle physics.—We consider 1D Fermi gases with two internal states (labeled by $\sigma = \uparrow, \downarrow$) tightly confined in transverse directions [Fig. 1(a)]. Two counter-propagating laser beams (wavelength λ) form a main optical lattice $V_0(x) = V_0 \cos^2(k_0 x)$ with $k_0 = 2\pi/\lambda$. Two additional laser beams (wavelength λ') incident at a tilt angle θ_0 form a secondary weak lattice $V_2(x) = V_2 \cos^2(k_2 x + \varphi)$ with $k_2 = 2\pi \cos \theta_0 / \lambda'$ and relative phase φ with respect to the main lattice. As illustrated in Fig. 1(b), the total potential $V(x) = V_0(x) + V_2(x)$ forms a superlattice, with its period determined by the ratio $q = k_0/k_2 = \frac{\lambda'}{\lambda \cos \theta_0}$. Such optical superlattice has been experimentally realized by many groups [17–19].

When the potential depth V_0 is much larger than the recoil energy $E_r = \hbar^2 k_0^2 / 2M$ (M is the atomic mass), only the lowest Bloch band need be considered and the system can be well approximated [20–23] by the following

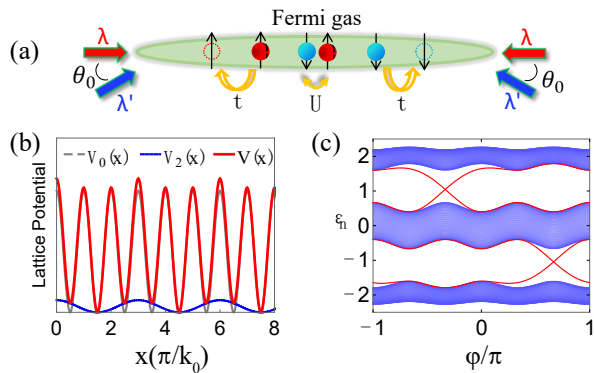


FIG. 1: (a) Schematic of experimental setup. A two-component Fermi gas is confined in 1D. Two counter-propagating red lasers (wavelength λ) form the main lattice, while two blues lasers (λ') incident at an angle θ_0 form the secondary weak long period lattice. (b) Resulting lattice potential. The local minima of the total potential are located at the minima of the main lattice. (c) Single-particle bands under OBC. Red lines highlight the end modes. $q = 3$, $\mu = 1.2$, $L = 240$.

tight-binding model with a superlattice potential

$$H = \sum_{j=1, \sigma}^L [-t(c_{j\sigma}^\dagger c_{j+1\sigma} + h.c.) + \mu_j n_{j\sigma}] + U n_{j\uparrow} n_{j\downarrow}, \quad (1)$$

where $c_{j\sigma}$ annihilates a spin- σ fermion at j -th site, L is the length of the chain, and $\mu_j = \mu \cos(2\pi j/q + \varphi)$ is the on-site long period superlattice potential. Hereafter $t = 1$ is set as the energy unit. A cyclical variation of φ brings back the Hamiltonian $H(\varphi) = H(\varphi + 2\pi)$, which is crucial for topological Thouless pumping [24] and the evolution of edge modes. The interaction U between atoms can be tuned over a wide range via Feshbach resonance or confinement induced resonance [25] for 1D systems. At half-filling, the Hamiltonian remains invariant under the simultaneous transformations $\varphi \rightarrow \varphi + \pi$ and $c_{j\sigma} \rightarrow c_{j\bar{\sigma}}^\dagger$, resulting in an energy spectrum of period- π on φ .

In this paper, we elaborate on $q = 3$ case and the generalization to other periods is straightforward. For incommensurate case, the interaction can induce many-body localization [19]. Since each unit cell has three sites, the single-particle spectrum contains three bands [Fig. 1(c)]. Different from normal insulator, there are end modes connecting adjacent bands in each gap under open boundary condition (OBC). Under periodical boundary condition (PBC), these end modes merge into bulk bands and disappear. The nontrivial band topology is characterized by the topological invariant Chern number [8–14]

$$\mathcal{C} = \frac{1}{2\pi} \iint d\theta d\varphi F(\theta, \varphi) \quad (2)$$

formulated in the 2D parameter space spanned by $(\theta, \varphi) \in [0, 2\pi] \times [0, 2\pi]$, where θ is introduced by imposing a twist boundary condition [26, 27] $\Psi_{j+L} = \Psi_j e^{i\theta}$

on the wave function, $F(\theta, \varphi) = \text{Im}(\langle \frac{\partial \Psi}{\partial \varphi} | \frac{\partial \Psi}{\partial \theta} \rangle - \langle \frac{\partial \Psi}{\partial \theta} | \frac{\partial \Psi}{\partial \varphi} \rangle)$ is the Berry curvature. $\mathcal{C} = 1$ and -1 when the chemical potential lies in the first and second band gaps, respectively. According to bulk-edge correspondence, the Chern number is equal to the number of chiral edge states by adiabatically evolving φ , as long as the bulk gap remains finite in the whole process [24, 28–30].

Topological Mott transition and SCS.—Now we consider an interacting many-body system $(N_\uparrow, N_\downarrow)$, composed of N_\uparrow spin-up and N_\downarrow spin-down atoms. Both total density $\rho = \sum_{j, \sigma} n_{j\sigma}/L$ and magnetization $m = \sum_j (n_{j\uparrow} - n_{j\downarrow})/L$ are conserved quantities. We denote the n -th lowest eigenenergy and corresponding wave function as $E_n(N_\uparrow, N_\downarrow)$ and $\Psi_n(N_\uparrow, N_\downarrow)$, respectively. $n = 0$ then refers to the many-body ground state. In the subsequent DMRG calculations, density-matrix eigenstates are kept dynamically to ensure the discarded weight less than 10^{-9} . The maximum truncation error of the ground state energy is about 10^{-7} and in general 10–15 sweeps are enough to reach the required precision.

We utilize three different bulk excitation gaps to characterize the low-energy modes: charge gap $\Delta_c = [E_0(N_\uparrow + 1, N_\downarrow + 1) + E_0(N_\uparrow - 1, N_\downarrow - 1) - 2E_0(N_\uparrow, N_\downarrow)]/2$ with a fixed magnetization m , spin gap $\Delta_s = [E_0(N_\uparrow + 1, N_\downarrow - 1) + E_0(N_\uparrow - 1, N_\downarrow + 1) - 2E_0(N_\uparrow, N_\downarrow)]/2$ with a fixed density ρ , and neutral gap $\Delta_{ne} = E_1(N_\uparrow, N_\downarrow) - E_0(N_\uparrow, N_\downarrow)$. The neutral gap directly gives the lowest excitation energy of the many-body system $(N_\uparrow, N_\downarrow)$.

We concentrate on the half-filling case with $\rho = 1$, $m = -1/3$. In the non-interacting limit, two-component fermionic atoms populate single-particle levels from low to high independently as sketched in Fig. 2(a). The spin-up atoms are filled up to the first band gap (denoted as δ_1) and spin-down atoms to the second band gap (denoted as δ_2). Because two band gaps are characterized by opposite Chern numbers $\mathcal{C} = \pm 1$, the system is in a quantum spin Hall-like state with a spin Chern numbers $\mathcal{C}_s = 2$ [31, 32] that is defined by Eq. (2) through choosing $\theta_\uparrow = -\theta_\downarrow$ for the twisted boundary condition. Here a single-particle excitation should overcome the band gaps and carry both charge and spin degree of freedom. The spin and charge gaps are equal, determined by: $\Delta_s = \Delta_c = (\delta_1 + \delta_2)/2$ because spin and charge modes are tightly bound together. $\Delta_{ne} = \min\{\delta_1, \delta_2\}$ in this case.

With increasing interaction, the spin and charge modes would exhibit totally different behaviors. Fig. 2(b) plots the three gaps with respect to U . Due to the repulsion between different components, the atoms prefer occupying higher levels. Starting from the same value, both Δ_c and Δ_s decrease first. Δ_c arrives its minimum at $U_c \approx 2.9$, where Δ_{ne} closes. Δ_c and Δ_s coincide with each other at $U < U_c$, revealing that spin and charge modes are coupled together. After the critical point, an obvious separation between spin and charge excitations happens. Δ_c grows rapidly (linearly) by further increasing U , whereas

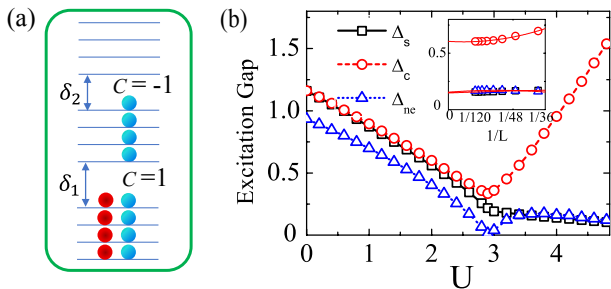


FIG. 2: (a) Sketch of level occupation in non-interacting limit with $\rho = 1$, $m = -1/3$. δ_1 and δ_2 denote the single-particle band gaps, characterized by $\mathcal{C} = \pm 1$, respectively. (b) The spin gap Δ_s (black square), charge gap Δ_c (red circle), and neutral gap Δ_{ne} (blue triangle) with respect to interaction U . The inset shows finite-size analysis of three gaps. The red lines are from polynomial fitting. $U = 3.5$, $\mu = 1.2$, $\varphi = 0$.

Δ_s is suppressed (with $1/U$). Note that none of the three excitation gaps can close for any $U > U_c$, and the system enters into a Mott insulator phase, with every lattice sites being populated at $U \rightarrow \infty$. Since the low-energy excitation now possesses only spin degree of freedom, Δ_{ne} coincides with Δ_s in this regime, as clearly demonstrated by our numerical results. To rule out the size effect, we do a finite-size scaling of different gaps after Mott transition. As shown in the inset of Fig. 2(b), Δ_c and Δ_s (Δ_{ne}) both tend to finite values in thermodynamic limit, which is crucial for the protection of non-trivial topological properties.

The Mott transition at $U = U_c$ is of first-order, with gap closing between ground and first excited states. Lattice translation symmetry forces $E_n(\varphi) = E_n(\varphi + \pi/3)$ at $\rho = 1$, therefore there are six gap closing points $\varphi_p = p\pi/3$ ($0 \leq p \leq 5$ is an integer) in the whole evolution period of $\varphi \in [0, 2\pi]$. Across the Mott transition, the spin Chern number changes six from $\mathcal{C}_s = 2$ to $\mathcal{C}_s = -4$, in consistent with simultaneous gap closing at six φ_p .

The Mott transition is accompanied with SCS. After the transition, the Hamiltonian can be represented by two distinct sectors $H = H_c + H_s$. While the charge sector H_c is fully gapped out due to the strong interaction, the low-energy physics is governed by an effective spin sector H_s . A second-order perturbation theory at large U leads to an antiferromagnetic spin superexchange Hamiltonian [33]

$$H_s = \sum_j J \left[1 + \frac{(\mu_{j+1} - \mu_j)^2}{U^2} \right] \mathbf{S}_j \cdot \mathbf{S}_{j+1} \quad (3)$$

with periodically modulated exchange couplings. Here $\mathbf{S}_j = c_j^\dagger \boldsymbol{\sigma} c_j / 2$ is the local spin operator at j -th site. $J = 4t^2/U$ is the key energy scale of Mott physics. Δ_{ne} (Δ_s) decreases by $1/U$ to the leading order. From the standard bosonization theory [34], $m = -1/3$ is a quantized magnetization plateau that is topologically pro-

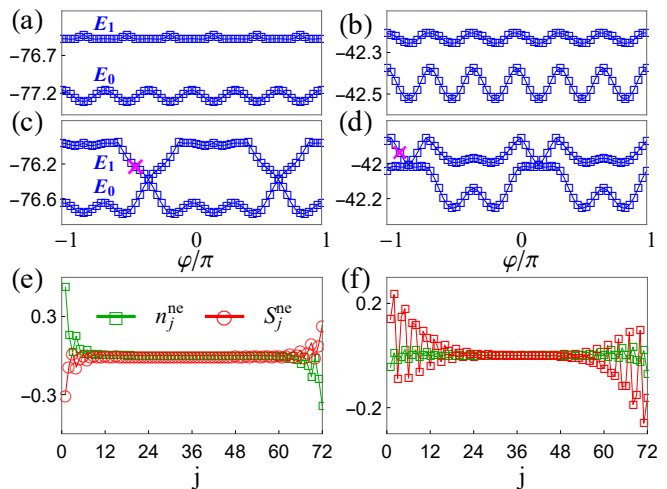


FIG. 3: The evolution of low-energy spectrum with φ for $\rho = 1$, $m = -1/3$ under (a) PBC; (c) OBC for $U = 1$ and (b) PBC; (d) OBC for $U = 3.5$. (e) and (f) represent the spatial distributions of charge n_j^{ne} (blue square) and spin S_j^{ne} (red circle) for the chosen neutral excitation modes [shown by “cross” in (c) and (d)], respectively. $U = 3.5$. $\mu = 1.2$.

tected [13]. All non-trivial properties can be understood from the above low-energy theory [33].

Bulk-edge correspondence.—The appearance of edge states is usually considered as a hallmark of topological properties. As SCS has severely changed the nature of low-energy excitations, bulk-edge correspondence of a topological Mott state is different. To this end, we study the low-energy spectrum under OBC and demonstrate the consequence of SCS. The charge distribution of a neutral excitation is $n_j^{ne} = n_j[\Psi_1(N_\uparrow, N_\downarrow)] - n_j[\Psi_0(N_\uparrow, N_\downarrow)]$. Here $[\Psi]$ represents for taking expectation value on state Ψ and $n_j = n_{j\uparrow} + n_{j\downarrow}$. Similarly, the spin distribution of a neutral excitation is $S_j^{ne} = S_j^z[\Psi_1(N_\uparrow, N_\downarrow)] - S_j^z[\Psi_0(N_\uparrow, N_\downarrow)]$ with $S_j^z = (n_{j\uparrow} - n_{j\downarrow})/2$. For each end, the accumulated charge (spin) is $n_l^{ne}(S_l^{ne}) = \sum_{j < L/2} n_j^{ne}(S_j^{ne})$, and $n_r^{ne}(S_r^{ne}) = \sum_{j > L/2} n_j^{ne}(S_j^{ne})$, respectively.

Our results are summarized in Fig. 3. Before SCS, there exist gapless modes inside the neutral gap under OBC by advancing φ . While prohibited under PBC [Fig. 3(a)], the ground state and first excited state cross at $\varphi = -\pi/3, 2\pi/3$ under OBC as shown in Fig. 3(c), indicating these modes are localized end modes. The crossings are reminiscent of the level crossings of single-particle levels in Fig. 1(c). Fig. 3(e) plots the spatial distributions of spin and charge for one of the in-gap neutral excitations. It is clear that the excitation carries both spin and charge at two ends. Our numeric shows $n_l^{ne} = 1$, $S_l^{ne} = -1/2$ for the left end and vice versa for the right end, which is in agreement with the bulk spin Chern number $\mathcal{C}_s = 2$ and validates the single-particle nature of these low-energy modes.

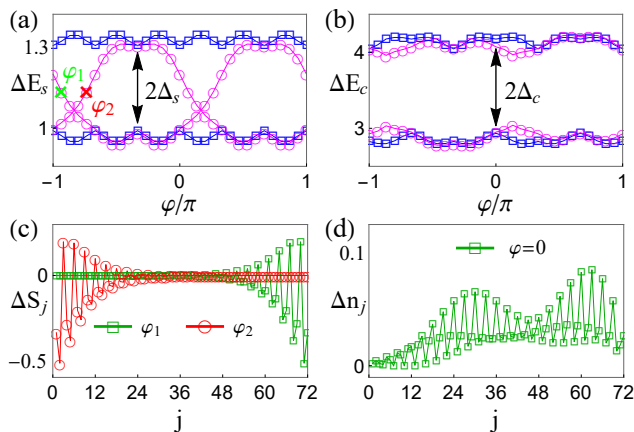


FIG. 4: (a) Magnon spectrum $\Delta E_s(24, 48)$ and $\Delta E_s(25, 47)$ at filling $\rho = 1$. The blue and magenta points are for PBC and OBC, respectively. (b) Charge spectrum $\Delta E_c(24, 48)$ and $\Delta E_c(23, 47)$ for magnetization $m = -1/3$. (c) Spatial distributions ΔS_j for two in-gap magnon modes [labeled by “cross” in (a)]. (d) Spatial distributions Δn_j for the charge excitation at $\varphi = 0$. $\mu = 1.2$, $U = 3.5$. The double-headed arrows denote the spin and charge gaps.

After SCS, the low-energy spectrum is fully gapped under PBC [Fig. 3(b)] and gapless end modes still emerge as shown in Fig. 3(d). Note that the appearance of these modes is at different φ 's ($\varphi = -5\pi/6, \pi/6$), which can be understood from the adiabatic continuity [33] of the effective spin Hamiltonian (3). $n_{l,r}^{ne} = 0$, and $S_{l,r}^{ne} = \pm 1$ for left and right ends (Fig. 3(f)). These two pairs of spin-1 edge modes are in consistent with bulk $C_s = -4$.

Topological magnon excitation.—The spin-1 low-energy excitations after SCS indicates the existence of pure collective magnon edge excitations in the spin sector. Starting from the many-body ground state $\Psi_0(N_\uparrow, N_\downarrow)$, the magnon spectrum is defined as $\Delta E_s(N_\uparrow, N_\downarrow) = E_0(N_\uparrow - 1, N_\downarrow + 1) - E_0(N_\uparrow, N_\downarrow)$ by fixing the total density of the system, with spatial spin distribution $\Delta S_j = S_j^z[\Psi_0(N_\uparrow - 1, N_\downarrow + 1)] - S_j^z[\Psi_0(N_\uparrow, N_\downarrow)]$ and no charge. Similarly, we define charge spectrum with fixed magnetization as $\Delta E_c(N_\uparrow, N_\downarrow) = E_0(N_\uparrow + 1, N_\downarrow + 1) - E_0(N_\uparrow, N_\downarrow)$ and associated spatial distribution as $\Delta n_j = n_j[\Psi_0(N_\uparrow + 1, N_\downarrow + 1)] - n_j[\Psi_0(N_\uparrow, N_\downarrow)]$.

In Fig. 4(a)(b), we show these two spectra after Mott transition, respectively. A magnon gap ($\sim 2\Delta_s$) separates the magnon bands under PBC, whereas in-gap modes under OBC cross at $\varphi = -5\pi/6$ and $\pi/6$ [Fig. 4(a)], same as the neutral excitations in Fig. 3(d). The distributions of magnon excitations in two typical phases $\varphi = -14\pi/15$, $\varphi = -11\pi/15$ are shown in Fig. 4(c), which are well localized end modes. Once touching the bulk band, they merge into the bulk and reappear on the other end. The non-trivial magnon excitations are closely related to the quantized magnetization plateau [13] of our effective model (3). For the charge spectrum

in Fig. 4(b), a charge gap ($\sim 2\Delta_c$) always exists regardless of boundary conditions. For any φ , the charge excitations distribute on the whole lattice [Fig. 4(d)], revealing the triviality in the charge sector.

Discussion and summary.—Our mechanism of inducing topological Mott insulator states based on SCS is quite general. The topological Mott physics here can be extended to i) other period- q (including incommensurate case, *i.e.*, the famous Aubry-André model [35]); ii) other fillings or magnetizations; iii) off-diagonal counterparts of model (1), *i.e.*, triple-well lattices with period modulations on tunneling t , instead of on-site energy μ_j . The emergence of topological Mott insulator states with various spin Chern numbers and spinful edge modes is expected from our low-energy theory.

The proposed topological Mott insulator state and associated low-energy excitations can be experimentally probed in ultracold atomic gases. In addition to the proposed scheme using two sets of optical lattices, the 1D fermionic superlattice can also be generated using the recently developed digital micromirror device [36, 37]. For fermionic ${}^6\text{Li}$ atoms [38, 39], the wavelength of the laser beam is chosen as $\lambda = 1064$ nm, with the recoil energy $E_r \approx 2\pi\hbar \times 29.4$ kHz. At $V_0/E_r = 5$, $t \approx 2\pi\hbar \times 1.9$ kHz. The neutral and spin gaps of the topological Mott insulator state is then $\Delta_{ne} \approx 0.2t = 2\pi\hbar \times 390$ Hz, which is large enough (compared to temperature) to protect the topological properties [39]. These excitation gaps may be measured using radio-frequency spectroscopy [40–42]. The edge magnon excitations in the spin sector can be generated using a two-photon Raman process and their spin distributions at each site can be measured by detecting atomic spin distributions of different many-body ground states using spin-resolved quantum gas microscope [43–48] in optical lattices.

In summary, we have studied topological Mott transitions accompanied by SCS in a simple 1D optical superlattices, with low-energy excitations changing from single-particle spin-1/2 modes to bosonic spin-1 collective modes at the boundary. A novel topological Mott insulator state, characterized by spin Chern number and gapless magnon excitations is identified. Our work may pave the way for the experimental observation of topological Mott insulator states in ultracold atomic gases.

Acknowledgments: We would like to thank Fan Zhang for helpful discussions. This work is supported by NSF (PHY-1505496), ARO(W911NF-17-1-0128), AFOSR (FA9550-16-1-0387). S C is supported by the National Key Research and Development Program of China (2016YFA0300600) and NSFC under Grants No. 11425419 and No. 11374354.

* Electronic address: chuanwei.zhang@utdallas.edu

- [1] M. Z. Hasan and C. L. Kane, *Colloquium: Topological insulators*, *Rev. Mod. Phys.* **82**, 3045 (2010).
- [2] X.-L. Qi and S. C. Zhang, *Topological insulators and superconductors*, *Rev. Mod. Phys.* **81**, 109 (2009).
- [3] D. C. Tsui, H. L. Stormer, and A. C. Gossard, *Two-dimensional magnetotransport in the extreme quantum limit*, *Phys. Rev. Lett.* **48**, 1559 (1982).
- [4] R. B. Laughlin, *Anomalous quantum Hall effect: An incompressible quantum fluid with fractionally charged excitations*, *Phys. Rev. Lett.* **50**, 1395 (1983).
- [5] S. Raghu, X.-L. Qi, C. Honerkamp, and S.-C. Zhang, *Topological Mott insulators*, *Phys. Rev. Lett.* **100**, 156401 (2008).
- [6] D. Pesin, L. Balents, *Mott physics and band topology in materials with strong spin-orbit interaction*, *Nat. Phys.* **6**, 376 (2010).
- [7] T. Yoshida, R. Peters, S. Fujimoto, and N. Kawakami, *Characterization of a topological Mott insulator in one dimension*, *Phys. Rev. Lett.* **112**, 196404 (2014).
- [8] L.-J. Lang, X. M. Cai, and S. Chen, *Edge states and topological phases in one-dimensional optical superlattices*, *Phys. Rev. Lett.* **108**, 220401 (2012).
- [9] Y. E. Kraus, Y. Lahina, Z. Ringel, M. Verbin, and O. Zeitlinger, *Topological states and adiabatic pumping in quasicrystals*, *Phys. Rev. Lett.* **109**, 106402 (2012).
- [10] S.-L. Zhu, Z.-D. Wang, U.-H. Chan, and L.-M. Duan, *Topological Bose-Mott insulators in a one-dimensional optical superlattice*, *Phys. Rev. Lett.* **110**, 075303 (2013).
- [11] Z. H. Xu, L. H. Li, and S. Chen, *Fractional topological states of dipolar fermions in one-dimensional optical superlattices*, *Phys. Rev. Lett.* **110**, 215301 (2013).
- [12] Z. H. Xu and S. Chen, *Topological Mott insulators of ultracold atomic mixtures induced by interactions in one-dimensional optical superlattices*, *Phys. Rev. B* **88**, 045110 (2013).
- [13] H. P. Hu, C. Cheng, Z. H. Xu, H.-G. Luo, and S. Chen, *Topological nature of magnetization plateaus in periodically modulated quantum spin chains*, *Phys. Rev. B* **90**, 035150 (2014).
- [14] H. P. Hu, H. M. Guo, and S. Chen, *Fractional topological states in quantum spin chains with periodical modulation*, *Phys. Rev. B* **93**, 155133 (2016).
- [15] D. R. Hofstadter, *Energy levels and wave functions of Bloch electrons in rational and irrational magnetic fields*, *Phys. Rev. B* **14**, 2239 (1976).
- [16] P. G. Harper, *The general motion of conduction electrons in a uniform magnetic field, with application to the diamagnetism of metals*, *Proc. Phys. Soc. A* **68**, 874 (1955).
- [17] G. Roati et al., *Anderson localization of a non-interacting Bose-Einstein condensate*, *Nature* **453**, 895 (2008).
- [18] L. Fallani, J. E. Lye, V. Guarrera, C. Fort, and M. Inguscio, *Ultracold atoms in a disordered crystal of light: towards a Bose glass*, *Phys. Rev. Lett.* **98**, 130404 (2007).
- [19] M. Schreiber et al., *Observation of many-body localization of interacting fermions in a quasirandom optical lattice*, *Science* **349**, 842 (2015).
- [20] V. Guarrera, L. Fallani, J. E. Lye, C. Fort, and M. Inguscio, *Inhomogeneous broadening of a Mott insulator spectrum*, *New J. Phys.* **9**, 107 (2007).
- [21] G. Roux et al., *Quasiperiodic Bose-Hubbard model and localization in one-dimensional cold atomic gases*, *Phys. Rev. A* **78**, 023628 (2008).
- [22] B. Damski, J. Zakrzewski, L. Santos, P. Zoller, and M. Lewenstein, *Atomic Bose and Anderson glasses in optical lattices*, *Phys. Rev. Lett.* **91**, 080403 (2003).
- [23] T. Roscilde, *Bosons in one-dimensional incommensurate superlattices*, *Phys. Rev. A* **77**, 063605 (2008).
- [24] D. J. Thouless, *Quantization of particle transport*, *Phys. Rev. B* **27**, 6083 (1983).
- [25] M. Olshanii, *Atomic scattering in the presence of an external confinement and a gas of impenetrable bosons*, *Phys. Rev. Lett.* **81**, 938 (1998).
- [26] D. Xiao, M.-C. Chang, and Q. Niu, *Berry phase effects on electronic properties*, *Rev. Mod. Phys.* **82**, 1959 (2010).
- [27] Q. Niu, D. J. Thouless, and Y.-S. Wu, *Quantized Hall conductance as a topological invariant*, *Phys. Rev. B* **31**, 3372 (1985).
- [28] Y. Qian, M. Gong, C. Zhang, *Quantum transport of bosonic cold atoms in double well optical lattices*, *Phys. Rev. A* **84**, 013608 (2011).
- [29] L. Wang, M. Troyer, and X. Dai, *Topological charge pumping in a one-dimensional optical lattice*, *Phys. Rev. Lett.* **111**, 026802 (2013).
- [30] S. Nakajima et al., *Topological Thouless pumping of ultracold fermions*, *Nat. Phys.* **12**, 296 (2016).
- [31] D. N. Sheng, L. Balents, and Z. Q. Wang, *Phase diagram for quantum Hall bilayers at $\nu = 1$* , *Phys. Rev. Lett.* **91**, 116802 (2003).
- [32] D. N. Sheng, Z. Y. Weng, L. Sheng, and F. D. M. Haldane, *Quantum spin-Hall effect and topologically invariant Chern numbers*, *Phys. Rev. Lett.* **97**, 036808 (2006).
- [33] See “Supplementary materials” for the derivation of low-energy Hamiltonian and discussion on its topological properties.
- [34] M. Oshikawa, M. Yamanaka, and I. Affleck, *Magnetization plateaus in spin chains: “Haldane Gap” for half-integer spins*, *Phys. Rev. Lett.* **78**, 1984 (1997).
- [35] S. Aubry, G. André, *Ann. Israel Phys. Soc.* **3**, 133 (1980).
- [36] M. E. Tai et al., *Microscopy of the interacting Harper-Hofstadter model in the two-body limit*, *Nature* **546**, 519 (2017).
- [37] P. Zupancic et al., *Ultra-precise holographic beam shaping for microscopic quantum control*, *Opt. Express* **24**, 13881 (2016).
- [38] R. A. Hart et al., *Observation of antiferromagnetic correlations in the Hubbard model with ultracold atoms*, *Nature* **519**, 211 (2015).
- [39] A. Mazurenko et al., *A cold-atom Fermi-Hubbard antiferromagnet*, *Nature* **545**, 462 (2017).
- [40] C. Chin et al., *Observation of the pairing gap in a strongly interacting Fermi gas*, *Science* **305**, 1128 (2004).
- [41] G. K. Campbell et al., *Imaging the Mott insulator shells by using atomic clock shifts*, *Science* **313**, 649 (2006).
- [42] S. Kato et al., *Laser spectroscopic probing of coexisting superfluid and insulating states of an atomic Bose-Hubbard system*, *Nat. Commun.* **7**, 11341 (2016).
- [43] W. S. Bakr, J. I. Gillen, A. Peng, S. Fölling, and M. Greiner, *A quantum gas microscope for detecting single atoms in a Hubbard-regime optical lattice*, *Nature* **462**, 74 (2009).
- [44] J. F. Sherson et al., *Single-atom-resolved fluorescence imaging of an atomic Mott insulator*, *Nature* **467**, 68 (2010).
- [45] L. W. Cheuk et al., *Quantum-gas microscope for fermionic atoms*, *Phys. Rev. Lett.* **114**, 193001 (2015).
- [46] E. Haller et al., *Single-atom imaging of fermions in a quantum-gas microscope*, *Nat. Phys.* **11**, 738 (2015).
- [47] M. F. Parsons et al., *Site-resolved imaging of fermionic*

⁶*Li in an optical lattice*, *Phys. Rev. Lett.* **114**, 213002 (2015).

spin-correlation function in the Fermi-Hubbard model, *Science* **353**, 1253 (2016).

[48] M. F. Parsons et al., *Site-resolved measurement of the*

Supplementary Materials

Derivation of the effective spin superexchange model

We give a simple derivation of the effective spin superexchange model (3) in the main text using the second-order perturbation theory. To this end, we split the Hamiltonian (1) into two parts $H = Un_{j\uparrow}n_{j\downarrow} + H_{pert}$, with $H_{pert} = \sum_{j,\sigma} [-t(c_{j\sigma}^\dagger c_{j+1\sigma} + h.c.) + \mu_j n_{j\sigma}]$ as the perturbation term. For the half-filling case $\rho = 1$ and $U \gg t$, the local Hilbert space on sites j and $j + 1$ is spanned by the following four basis: $|\uparrow_j, \uparrow_{j+1}\rangle$, $|\uparrow_j, \downarrow_{j+1}\rangle$, $|\downarrow_j, \uparrow_{j+1}\rangle$, $|\downarrow_j, \downarrow_{j+1}\rangle$. The effective Hamiltonian can be represented in this basis as $H_s = \sum_j H_{j,j+1}$, with

$$H_{j,j+1} = \begin{pmatrix} 0 & 0 & 0 & 0 \\ 0 & -\frac{t^2}{U+\mu_{j+1}-\mu_j} - \frac{t^2}{U+\mu_j-\mu_{j+1}} & \frac{t^2}{U+\mu_{j+1}-\mu_j} + \frac{t^2}{U+\mu_j-\mu_{j+1}} & 0 \\ 0 & \frac{t^2}{U+\mu_{j+1}-\mu_j} + \frac{t^2}{U+\mu_j-\mu_{j+1}} & -\frac{t^2}{U+\mu_{j+1}-\mu_j} - \frac{t^2}{U+\mu_j-\mu_{j+1}} & 0 \\ 0 & 0 & 0 & 0 \end{pmatrix}. \quad (4)$$

Using spin-1/2 operator $\mathbf{S} = (S_x, S_y, S_z)$, the above Hamiltonian can be further represented as

$$H_s = \sum_j \frac{4t^2U}{U^2 - (\mu_{j+1} - \mu_j)^2} [\mathbf{S}_j \cdot \mathbf{S}_{j+1} - 1/4]. \quad (5)$$

By setting $J = \frac{4t^2}{U}$ and Taylor expanding the exchange coefficient by $1/U$ to the second term, we can get the effective spin superexchange model (3) after neglecting the constant term.

Adiabatic continuity and topological properties

Now we demonstrate the topological properties of the spin superexchange model, which dictates the low-energy physics of the system. To be more intuitive and clear, we introduce an anisotropy parameter g in $S_j^z S_{j+1}^z$ term:

$$H_s(g) = \sum_j J \left[1 + \frac{(\mu_{j+1} - \mu_j)^2}{U^2} \right] (S_j^x S_{j+1}^x + S_j^y S_{j+1}^y + g S_j^z S_{j+1}^z). \quad (6)$$

When $g = 1$, the above model recovers our low-energy Hamiltonian (3). $g = 0$ corresponds to an exactly solvable spin-XX chain by Jordan-Wigner transformation. We first show the non-trivial topology of $g = 0$ case and then demonstrate the adiabatic continuity in the whole region $g \geq 0$.

For $g = 0$, the Jordan-Wigner transformation (denote $S_k^\pm = S_k^x \pm iS_k^y$)

$$d_j^\dagger = e^{i\pi \sum_{k=1}^{j-1} S_k^+ S_k^-} \cdot S_j^+, \quad d_j = e^{-i\pi \sum_{k=1}^{j-1} S_k^+ S_k^-} \cdot S_j^-$$

takes the model (6) to a spinless fermion model: $H_{J-W} = \sum_j J \left[1 + \frac{(\mu_{j+1} - \mu_j)^2}{U^2} \right] (d_j^\dagger d_{j+1} + d_{j+1}^\dagger d_j)$. The band structure is shown in Fig. 5(a). Due to the periodically modulated hopping of Jordan-Wigner fermions, the single-particle spectrum ε_n^d consists of three topological bands and gapless end modes inside the band gap with the evolution of phase φ under OBC. Notice that different from the original single-particle band in Fig. 1, these end modes now cross at $\varphi = -5\pi/6$ and $\varphi = \pi/6$ (in consistent with the DMRG results in Fig. 3(b) and Fig. 4(a) in the main text) and represent for low-energy collective spinful modes.

To demonstrate the adiabatic continuity in the whole region $g \geq 0$, we plot the excitation gap (energy difference between the ground state and first excited state) of model (6) with respect to g in Fig. 5(b). With increasing g from Jordan-Wigner limit $g = 0$, the excitation gap increases. From the scaling behavior of the gap [Inset of Fig. 5(b)], we can see it tends to a finite value in thermodynamical limit at $g = 1$. The above adiabatic continuity reveals that our effective spin superexchange model H_s has the same topological properties with that of Jordan-Wigner fermions.

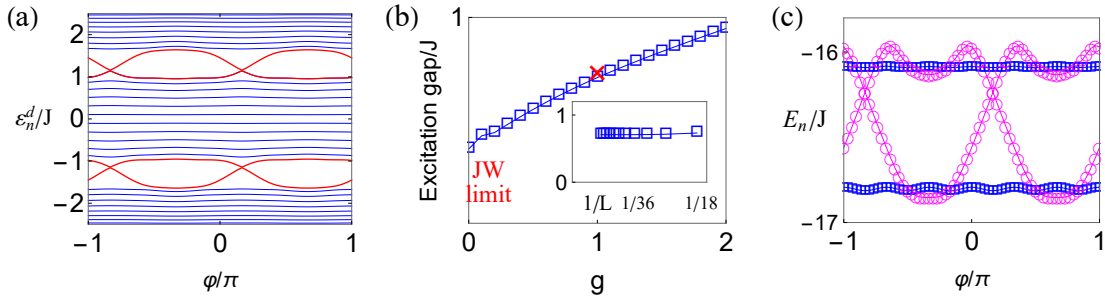


FIG. 5: (a) Single-particle band of Jordan-Wigner fermions, $g = 0$. (b) Excitation gap with respect to g . The inset shows the finite size scaling at $g = 1$, $\varphi = 0$. (c) The lowest two eigenenergies of model (6) under OBC (magenta circle) and PBC (blue square) with the evolution of φ . $\mu^2/U^2 = 0.2$ for all figures.

Furthermore, we show the low-energy spectrum of the spin superexchange model (3) in Fig. 5(c). Although there always exist an excitation gap at any φ under PBC, the ground state and first excited state touch at $\varphi = -5\pi/6$ and $\varphi = \pi/6$ under OBC (in consistent with the DMRG results in Fig. 3(b) and Fig. 4(a) in the main text). As these crossings depend on boundary condition, the excitations around the touching points are well localized end modes [not shown]. For example, at $\varphi = -9\pi/10$, our numeric gives accumulated spin distribution $\Delta S_z = 0.9996$ on the left end and $\Delta S_z = -0.9996$ on the right end. The integer spinful end modes are in consistent with those neutral excitations in the main text.